Natural metamaterial behavior across the phase transition for WxV1−xO2 films revealed by terahertz spectroscopy

Nicolas Émond, Badr Torriss, Denis Morris, Mohamed Chaker

Natural metamaterial behavior across the phase transition for $W_xV_{1-x}O_2$ films revealed by terahertz spectroscopy

Nicolas Émond [a, *], Badr Torriss [a], Denis Morris [b], Mohamed Chaker [a, **]

[a] *INRS-Énergie, Matériaux et Télécommunications, 1650, Boulevard Lionel Boulet, Varennes, Québec, J3X 1S2, Canada*
[b] *Département de Physique, Regroupement Québécois sur les Matériaux de Pointe, Université de Sherbrooke, Québec, J1K 2R1, Canada*

Metamaterials, which are made of repeated patterns of appropriately arranged small discrete structures, display unusual electromagnetic properties that overwhelm those of conventional materials. The modification of their properties is generally achieved by arranging the structures mechanically or electrically and requires rather complex designs. We report on the study of the complex conductivity of epitaxially-grown tungsten-doped vanadium dioxide ($W_xV_{1-x}O_2$) thin films through the semiconductor-to-metal phase transition (SMT) using terahertz time-domain spectroscopy. The modelling of the terahertz conductivity across $W_xV_{1-x}O_2$ SMT provides clear insights about the gradual nucleation of VO_2 metallic domains among the semiconducting host and evidences the presence of strong carrier confinement and enhanced absorption close to the transition temperature, leading to a strong capacitive response of the electrons. The evolution of the SMT is also strongly affected by W doping, which reduces the scattering time in the metallic state, lowers the transition onset temperature and extends the temperature range over which the transition occurs. The $W_xV_{1-x}O_2$ films thus forms an effective medium in the vicinity of the SMT and display the signature of a disordered metamaterial, which has significantly enhanced functionality thanks to its readily thermally-tunable properties over a wide range of temperatures close to room temperature.

1. Introduction

Metamaterials unusual electromagnetic properties, which are absent in nature and allow absorbing, enhancing or even bending electromagnetic waves, come from their internal structure rather than the matter that composed them. These materials are made of repeated patterns of small discrete structures, called unit cells, and they exhibit exotic properties as long as the unit cells are sufficiently small as compared to the wavelength of the incident signal [1]. It is thus the combination of the size, geometry and orientation of these cells that gives metamaterials their unique properties. These properties, which include optical magnetism [2] and negative refractive index [3], have already been exploited for optoelectronic applications such as cloaking [4] and subwavelength imaging [5]. More recently, there has been considerable interest for real-time manipulation of electromagnetic radiations using tunable metamaterials, which electromagnetic response can be triggered electrically [6] or mechanically [7]. These artificial materials are usually composed of complex metal-dielectric composite structures and their tunability requires sophisticated designs like hybrid metamaterial, micromachined reconfigurable metamaterial or folding patterns [8]. A more versatile approach to the architecture of metamaterials uses tunable materials which electromagnetic response can be thermally-triggered, such as vanadium dioxide (VO_2) [9], resulting in a significant simplification of the metamaterial design.

VO_2 is a model system to study the nature of semiconductor-to-metal transitions in correlated electron systems. A balance of both Peierls-type [10] lattice instability due to electron-phonon interaction and Mott-type [11] electron-electron correlations drives this material in a critical regime as it undergoes a first-order reversible phase transition from a high-temperature metallic state to a low-temperature semiconducting state when cooled down below its transition temperature (T_{SMT}) $\approx$ 68 °C [12]. This phase transition is accompanied by a hysteresis and associated with a reduction of

* Corresponding author.
** Corresponding author.
E-mail addresses: emondn@emt.inrs.ca (N. Émond), chaker@emt.inrs.ca (M. Chaker).

crystal symmetry from a rutile phase (R) to a monoclinic phase (M), a sharp increase in electrical conductivity of close to 5 orders of magnitude and significant changes in optical properties [13]. Recent experiments on VO_2 films reveal that the semiconductor-to-metal transition first occurs at the nanoscale in spatially separated metallic puddles [14]. These strongly correlated conducting puddles, with an electromagnetic response that displays the signatures of collective effects in the electronic system, then grow and coalesce among the semiconducting host as the temperature increases so that their coexistence covers several length scales [15]. The connection between these metallic puddles across the VO_2 SMT further leads to the transition of the film electronic response from capacitive to inductive [16] and results in a metal-dielectric nanocomposite in the VO_2 thin film, which can thus be considered as a naturally-occurring metamaterial [17].

The SMT properties of VO_2 thin films strongly depend on stoichiometry, morphology and on the quality of the interface with the substrate [18,19]. Indeed, the SMT properties can efficiently be tailored by doping with an appropriate concentration of donors and/or acceptors. Doping with tungsten, the most efficient dopant element to lower VO_2 transition temperature, allows to reduce T_{SMT} by ~20 °C/at. % W [20], which is crucial for functionality around room temperature. This pronounced reduction is attributed to the introduction of extra electrons in the system and to the strong modification of the VO_2 local structure induced by substitutional doping. The W ions tend to bring the monoclinic short (~2.65 Å) and long (~3.12 Å) V-V dimers distances closer to the rutile uniform (~2.87 Å) V-V distance, thus activating conductivity [21].

Structural and morphological properties like strain, grain size, density of defects and grain boundaries also affect the SMT characteristics of VO_2 thin films, which can be tailored by a proper choice of the substrate and deposition conditions [22,23]. The VO_2 transition temperature is thus reduced/increased through compressive/tensile stress along the rutile c-axis due to lattice mismatch between film and substrate. Moreover, the SMT properties of VO_2 are strongly altered by the presence of defects and grain boundaries, which makes it crucial to synthesize thin films that exhibit high crystalline quality and SMT features similar to those of the bulk material for enhanced functionality. Substrates with different crystal structures have been used to grow high quality VO_2 thin films, including Al_2O_3, glass, TiO_2, $SrTiO_3$ and MgF_2 [24–26]. Among them, epitaxial VO_2 thin films deposited on Al_2O_3 $(1\bar{1}02)$ substrates are of particular interest as they exhibit high crystalline quality, SMT properties close to those of single crystal VO_2 and good transparency to far-infrared radiations [27].

The thermally-induced changes in the conductivity of the VO_2 thin films are associated with corresponding variations of the optical response, which makes terahertz spectroscopy (THz-TDS) a well-suited contactless technique to measure the complex conductivity and to study both the electron dynamics over nanometer length scales and the spatial inhomogeneity of the film induced by the formation of metallic domains. Therefore, its contactless nature is a significant advantage as opposed to standard dc conductivity measurements, which only probe long-range transport. So far, many researches on VO_2 films have focused on probing its optical THz conductivity and dielectric properties through the thermally-induced SMT in order to investigate the formation of the metallic state in the vicinity of the SMT [28,29]. Transient photoconductivity measurements have also been used to investigate the dynamic behavior of the photo-induced SMT in such VO_2 films: new insights on the thermal versus nonthermal effects as well as the interplay of electronic and lattice degrees of freedom during the phase transition were reported [30,31]. Despite the attractiveness of substituting vanadium atoms with W dopants in VO_2 lattice for functionality around room temperature, studies on the influence of VO_2 film doping in the terahertz range are still scarce [32,33] while its effect on the THz conductivity remains unexplored.

In this paper, we report on the investigation and modelling of the THz complex conductivity of 150-nm thick epitaxially-grown $W_xV_{1-x}O_2$ thin films deposited on Al_2O_3 $(1\bar{1}02)$ substrates across the SMT in the frequency range 0.25–1.55 THz using the Drude-Smith formalism. The absence of phonon resonance within this frequency range enables the study of the conductivity response of these films within their transitional state. Within this temperature range, they are formed of randomly dispersed metallic inclusions much smaller than the THz probing wavelength and can thus be assimilated to a naturally-occurring metamaterial with variable effective permittivity. Our study evidences that significant variations of Drude-Smith parameters are occurring across the SMT for the $W_xV_{1-x}O_2$ samples and clearly demonstrates differences in the evolution of the phase transition induced by the introduction of W dopants in the VO_2 lattice. The thermally-tunable THz properties of the $W_xV_{1-x}O_2$ films can be modified on a wide range of temperature close to room temperature without requiring any electrical or mechanical components. They therefore display enhanced functionality and are very attractive for optoelectronics applications.

2. Experimental

2.1. Sample growth

Reactive pulsed laser deposition (RPLD) was used to fabricate the $W_xV_{1-x}O_2$ thin films by ablating commercial undoped and tungsten-doped vanadium metal targets on *r*-cut oriented sapphire $(Al_2O_3(1\bar{1}02))$ substrate. The growth temperature was 550 °C and the oxygen pressure was kept at 21 mTorr. Detailed growth conditions were reported in a previous study [34].

2.2. XRD, AFM and electrical characterization

The structural properties of the films were examined by X-ray diffraction (XRD) in the θ–2θ configuration between 20° and 90° using a PANalytical's X'Pert PRO Materials Research Diffractometer with Cu Kα radiation operated at 45 kV and 40 mA. Film thickness was determined by cross-section scanning electron microscopy (SEM, JEOL JSM-7401F) observations while surface morphology was imaged by atomic force microscopy (AFM, DI-EnviroScope, Veeco). A standard four-point probe method was used to measure the

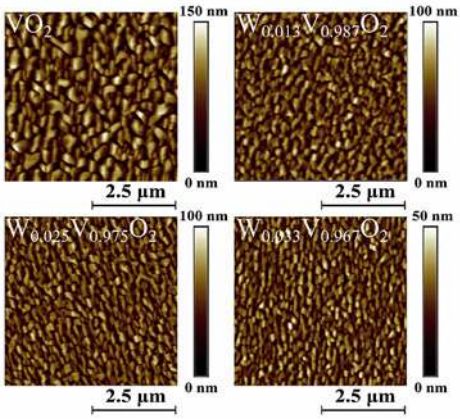

Fig. 1. AFM images of epitaxially-grown$W_xV_{1-x}O_2$ thin films.

resistivity of the films.

2.3. THz time-domain spectroscopy

Standard terahertz time-domain spectroscopy (THz-TDS) measurements were made between 0.25 THz and 1.55 THz and at temperatures ranging from −120 °C to 100 °C to investigate the temperature-dependent terahertz transmission of the films. For each set of experiments, two samples, the W-doped VO_2 film on sapphire substrate and the bare substrate, were mounted simultaneously on the cold finger of a liquid nitrogen cooled cryostat. Measurements were done in transmission. The THz-TDS setup was coupled to a Ti:sapphire regenerative amplifier that delivers 35 fs laser pulses with a central wavelength of 800 nm at a 1-kHz repetition rate. The laser beam was split into two distinct beams, an excitation beam used to generate the THz-probe beam, and a probing beam used to detect THz pulses transmitted through the sample. The 90 mW excitation beam generated the THz-probe beam by optical rectification in a 3 cm × 3 cm and 1 mm-thick ZnTe crystal. The THz radiation was focused on the sample surface on a spot diameter of about 2 mm using a parabolic mirror. The transmitted THz pulses were detected using electro-optic sampling in a 0.5-mm-thick ZnTe crystal. The THz-probe beam was chopped at 340 Hz and the THz signal was measured by means of a lock-in amplifier. The THz-probe beam was confined into a vacuum chamber and all measurements were performed at a pressure $<10^{-4}$ Torr.

3. Results

3.1. Morphological, structural and electrical characterization

The stoichiometry of the W-doped VO_2 films, determined from Rutherford backscattering spectrometry measurements, is $W_{0.013}V_{0.987}O_2$, $W_{0.025}V_{0.975}O_2$ and $W_{0.033}V_{0.967}O_2$. The AFM surface morphology images of $W_xV_{1-x}O_2$ thin films shown in Fig. 1 reveal the presence of large, compact and closely connected elongated grains. Tungsten doping significantly reduces the grain size from ≈260 nm for the VO_2 sample to ≈160 nm for the W-doped VO_2 samples, which accordingly results in higher density of grain boundaries. XRD data of the VO_2 film and of the $W_{0.033}V_{0.967}O_2$ film are shown in Fig. 2. Detailed analysis reveals that the peaks located at 37.1° and 79.1° correspond to the Bragg angle of $(200/\bar{2}11)_M$ and $(400/\bar{4}22)_M$ orientations respectively. All the other peaks coincide with reflection planes from the Al_2O_3 $(1\bar{1}02)$ substrate. The temperature-dependent DC electrical conductivity (σ_{DC}) of the VO_2 film for both heating and

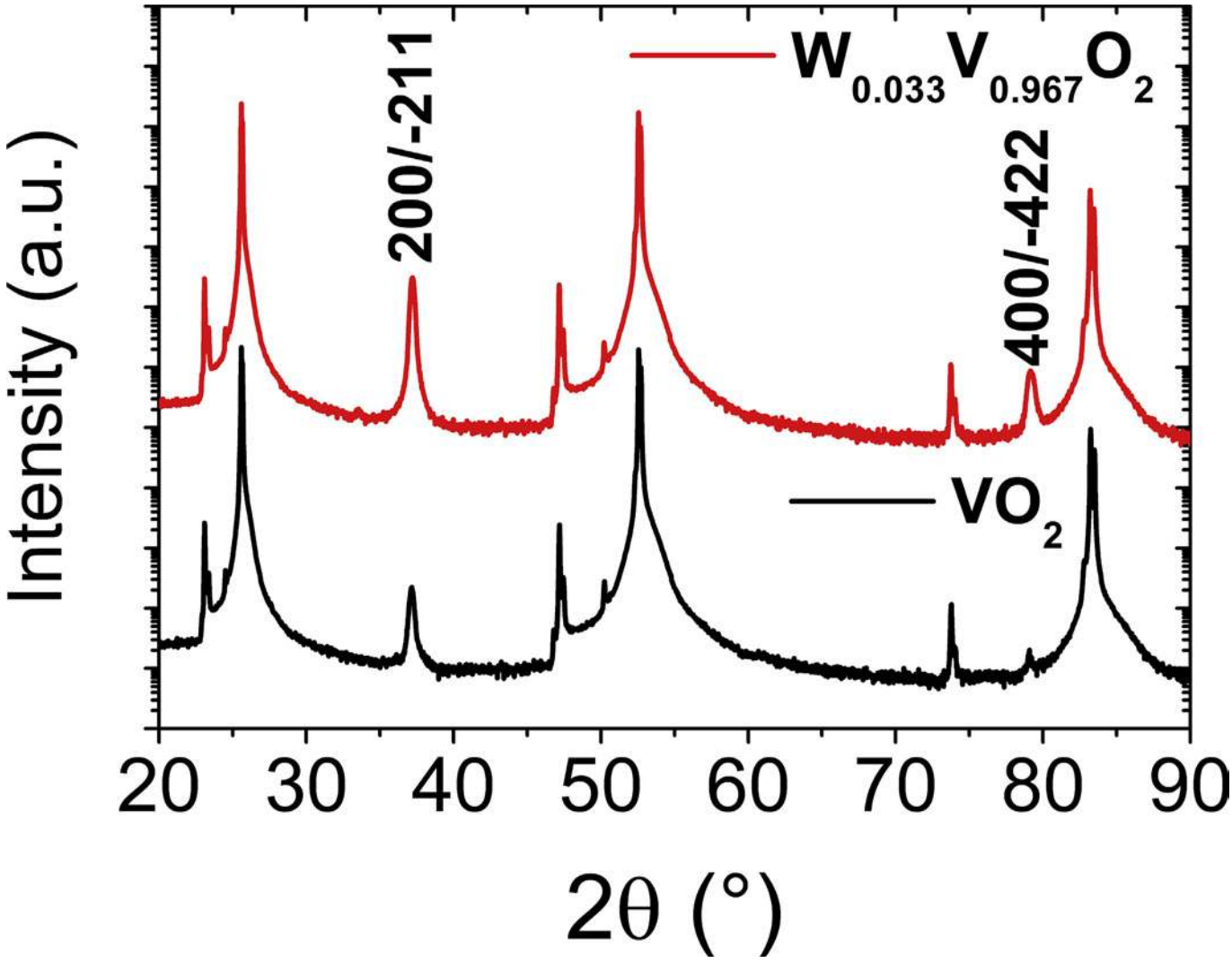

Fig. 2. XRD θ-2θ patterns for the VO_2 and $W_{0.033}V_{0.967}O_2$ thin films epitaxially grown on Al_2O_3 $(1\bar{1}02)$ substrates.

cooling segments is shown in Fig. 3A, where a sharp transition from the low temperature semiconducting phase to the high temperature metallic phase is observed at $T_{SMT} = 61.5$ °C. This transition is accompanied by a large contrast in conductivity $\Delta\sigma_{DC} = 99400$ between 20 °C and 95 °C and a small hysteresis $\Delta H = 4.1$ °C. Fig. 3B presents σ_{DC} of the $W_xV_{1-x}O_2$ films with various W concentrations as a function of temperature. A reduction of T_{SMT} with increasing the VO_2 films tungsten concentration is observed here. Also, the conductivity of the $W_xV_{1-x}O_2$ films saturates for temperatures above T_{SMT}, where the transition to the metallic state is completed. Tungsten doping does not noticeably alter the conductivity of the thin films in the metallic state. Indeed, similar conductivity values ranging from 1750 $(\Omega\ cm)^{-1} < (\sigma_{DC}) < 2550\ (\Omega\ cm)^{-1}$ are obtained for $W_xV_{1-x}O_2$ samples at high temperature.

3.2. THz time-domain spectroscopy

The THz waveforms of the pulses transmitted through the VO_2 film and the bare 500 μm-thick Al_2O_3 (1102) substrate were characterized independently. In Fig. 4, the time-domain THz signal transmitted through the VO_2 system (film + substrate) is compared to that of the reference (bare substrate) at temperatures below T_{SMT} ($T = 52$ °C) and above T_{SMT} ($T = 100$ °C). The Fast Fourier transform of the time-dependent THz waveforms, shown in the insets of Fig. 4, was performed to obtain the amplitude and phase of the THz spectra. No change of the THz signal between the VO_2 system and the reference is observed below T_{SMT} while at 100 °C, the THz signal transmitted through the VO_2 sample is drastically reduced. The frequency-dependent complex optical conductivity $(\tilde{\sigma}(\omega) = \sigma_1(\omega) + i\sigma_2(\omega))$ of the $W_xV_{1-x}O_2$ thin conductive films can be calculated by means of the Tinkham formula [35]:

$$\frac{\tilde{E}_{VO_2+substrate}(\omega)}{\tilde{E}_{substrate}(\omega)} = \frac{(1 + n_{substrate})}{(1 + n_{substrate} + Z_0\tilde{\sigma}(\omega)d)} \quad (1)$$

where $\tilde{E}_{VO_2+substrate}(\omega)$ and $\tilde{E}_{substrate}(\omega)$ correspond to the complex

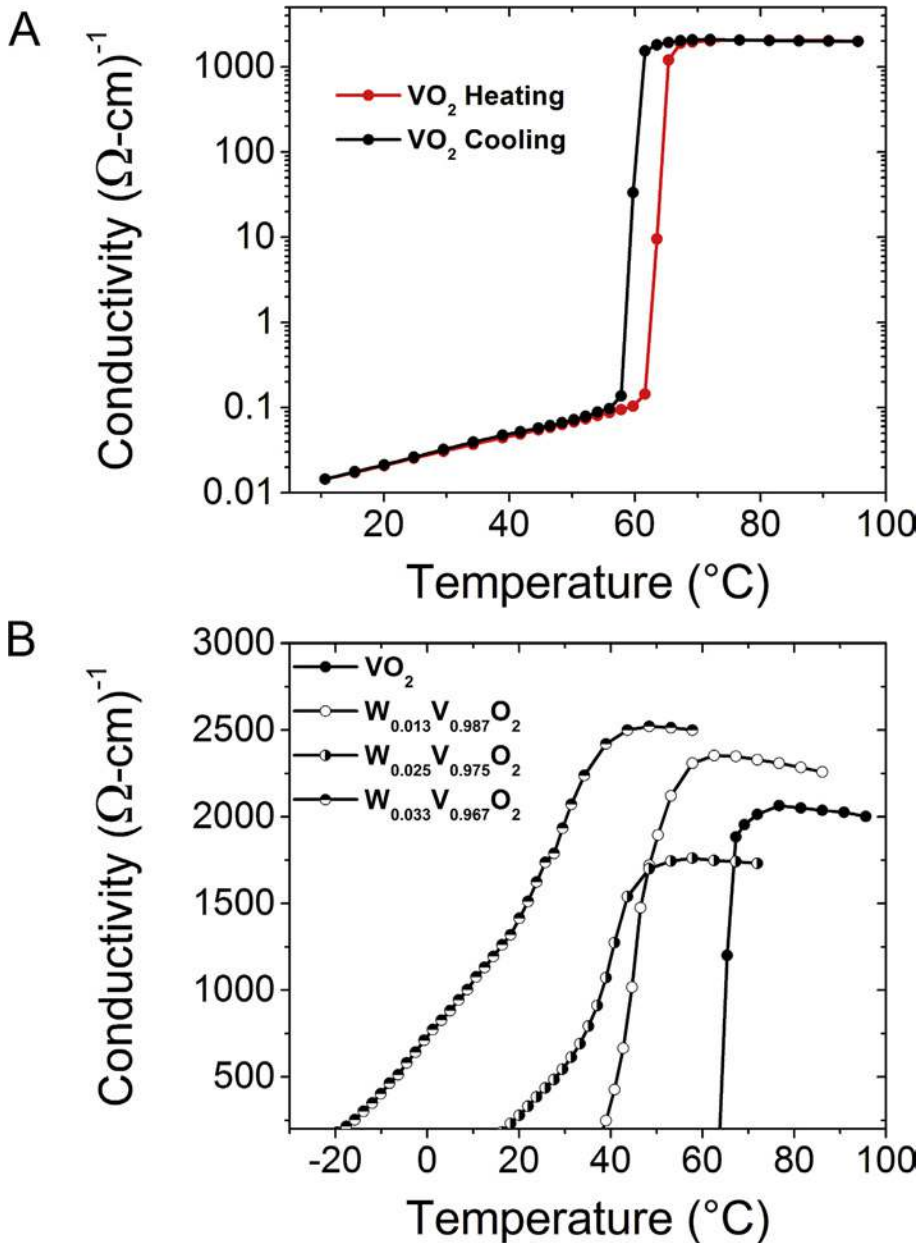

Fig. 3. Temperature-dependent DC conductivity of (A) the VO_2 thin film on Al_2O_3 ($1\bar{1}02$) for heating (red curve) and cooling (black curve) segments and (B) $W_xV_{1-x}O_2$ thin films on Al_2O_3 ($1\bar{1}02$) using a standard four point geometry. (For interpretation of the references to colour in this figure legend, the reader is referred to the web version of this article.)

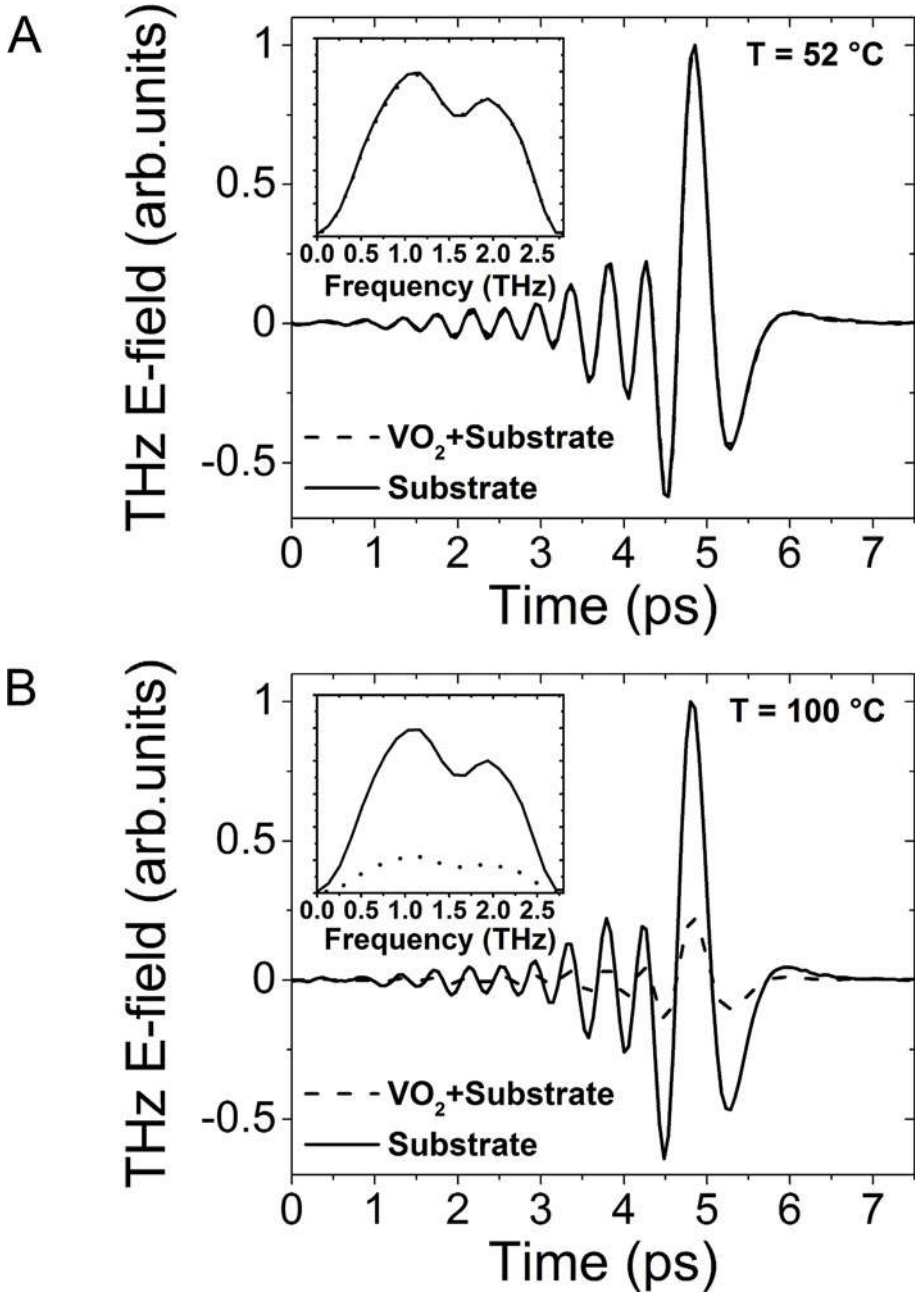

Fig. 4. THz waveforms transmitted through the Al_2O_3 $(1\bar{1}02)$ substrate and the Al_2O_3 $(1\bar{1}02)$ substrate + VO_2 film system at (A) 52 °C in the semiconducting state and (B) 100 °C in the metallic state during the heating segment. The insets show the complex Fourier transforms of the time-dependent terahertz fields, which corresponds to the pulse bandwidth.

electric field amplitude transmitted through the VO_2 system and to the reference respectively, Z_0 is the free space impedance, d is the film thickness and $n_{substrate} \approx 3.02$ is the nearly frequency-independent refractive index of the Al_2O_3 $(1\bar{1}02)$ substrate, which is thick enough to neglect the Fabry-Perot effect.

The temperature range over which the Tinkham formula is valid was determined considering the negligible optical thickness and the high conductivity criterion. First, negligible optical thickness requires that both $n\omega d/c \ll 1$ and $k\omega d/c \ll 1$ be satisfied [36], where n and k are the refractive index and the extinction coefficient of the film and c is the speed of light in free-space. For the VO_2 film at $T = 100$ °C, where the optical thickness is maximal, n decreases from 42 at 0.25 THz to 15 at 1.55 THz while k decreases from 40 at 0.25 THz to 16 at 1.55 THz. Thus, the maximum values of $n\omega d/c$ and $k\omega d/c$ are 0.07 and 0.08, respectively. Therefore, the two relations are valid over the whole range of temperature considered. Second, the approximation that neglects the lattice contribution $\varepsilon_L(\omega)$ in the complex permittivity $\tilde{\varepsilon}(\omega)$ of Eq. (2) requires that the VO_2 film is highly conductive.

$$\tilde{\varepsilon}(\omega) + 1 = \varepsilon_L(\omega) + i\tilde{\sigma}(\omega)/\omega\varepsilon_0 + 1 \approx i\tilde{\sigma}(\omega)/\omega\varepsilon_0 + 1 \quad (2)$$

here, ε_0 is the permittivity of free space. This criterion is linked to the thin film definition itself, which specifies that a film is too thin to be measured when it can no longer be distinguished from the reference material within the measurement uncertainty. A film is thus considered too thin to be measured if the standard deviation of its refractive index and extinction coefficient is larger than the

Table 1
Critical temperature (T_c) and refractive index (n) at two frequencies (0.25 and 1.55 THz) for VO_2 thin films with various W content.

W content (x)	0	0.013	0.025	0.033
Critical temperature T_c (°C)	59	39	17	−13
n at 0.25 THz	9.8	13.2	12.1	14.7
n at 1.55 THz	5.4	6.6	5.9	6.8

difference between the sample and the reference refractive indices and extinction coefficients. The following criterion is derived from these considerations [37]:

$$\frac{\omega d}{c}\Delta n(\omega) < \sqrt{\frac{2}{N}}s_{\arg(Eref)}(\omega) \quad (3)$$

where $\Delta n(\omega)$ is the difference between the real refractive index of the sample and $n_{substrate}$, $s_{\arg(Eref)}(\omega)$ is the standard deviation in the phase of the reference spectra and N is the number of scans performed at each temperature. When Eq. (3) is satisfied, the high conductivity criterion is no longer valid. As the refractive index n is decreasing with temperature, there exists a critical temperature T_c below which Eq. (3) starts to be fulfilled. This temperature is shown in Table 1 for each film composition. For each T_c value, the refractive index at 0.25 THz and 1.55 THz are also provided. Accordingly, extracting the complex conductivity of the $W_xV_{1-x}O_2$ films from THz-TDS measurements is valid for temperature equal to or higher than T_c.

3.3. Complex conductivity of $W_xV_{1-x}O_2$ thin films

The real (σ_1) and imaginary (σ_2) parts of the temperature-dependent THz optical conductivity of $W_xV_{1-x}O_2$ thin films were calculated from the complex Fourier transforms of the time-dependent fields using Eq. (1). Variations across the semiconductor-to-metal transition of both σ_1 and σ_2 are illustrated in Fig. 5. The value of σ_1 is seen to be frequency-independent but it decreases continuously all through the SMT as the temperature is reduced. On the other hand, σ_2 switches from positive values at high temperature (in the metallic phase) to negative values in the vicinity of the phase transition temperature (T_{SMT}) to finally reach a value smaller than 30 $(\Omega\ cm)^{-1}$ at low temperature (in the

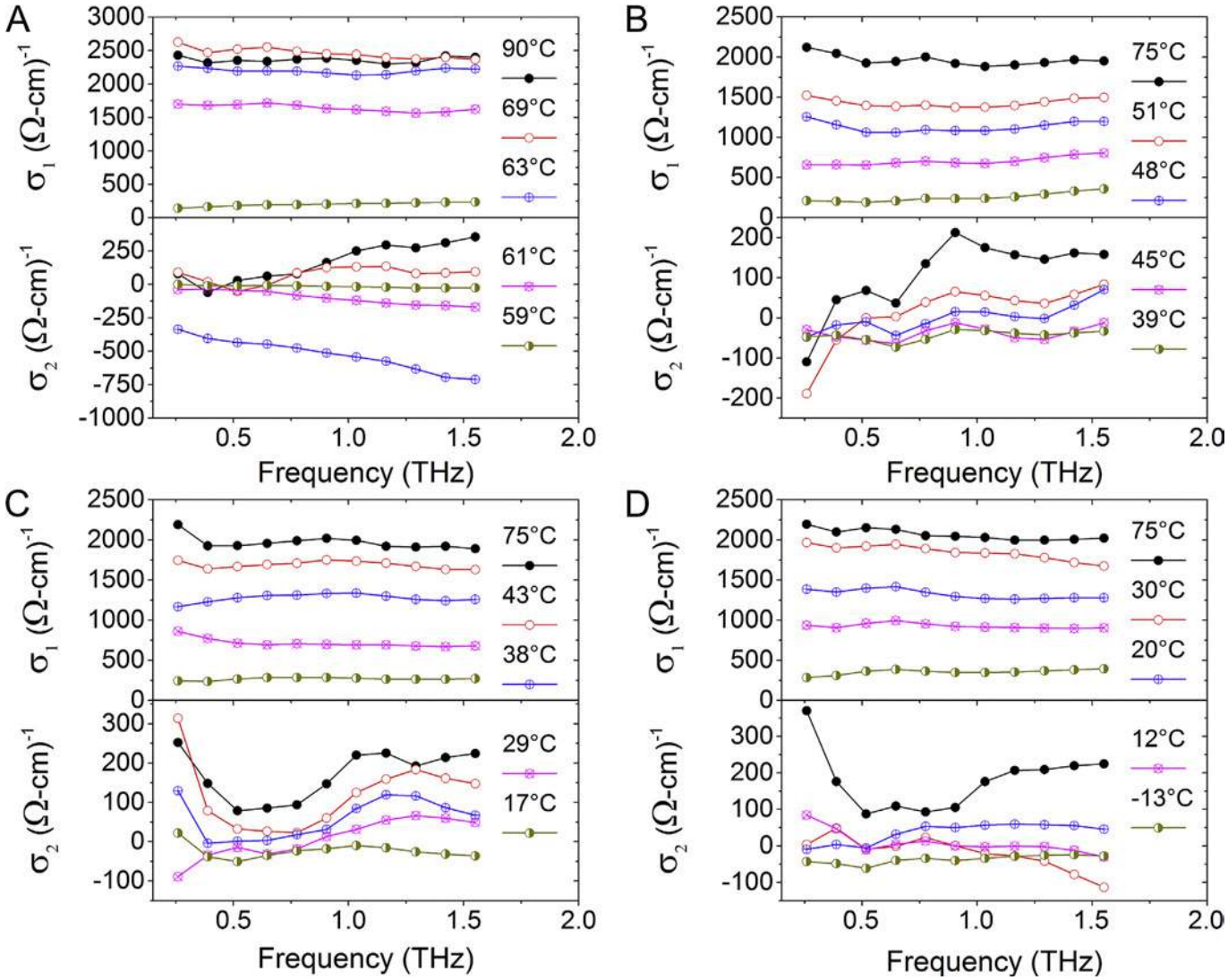

Fig. 5. Real (upper panel) and imaginary (lower panel) components of the THz conductivity of (A) VO_2 (B) $W_{0.013}V_{0.987}O_2$ (C) $W_{0.025}V_{0.975}O_2$ and (D) $W_{0.033}V_{0.967}O_2$ thin films at several temperatures across and above the phase transition during the heating segment.

semiconducting phase). The calculated values of σ_1 for all the $W_xV_{1-x}O_2$ films in the metallic phase are in close agreement with those of the DC conductivity measured using the four-point probe technique. The onset of a non-zero σ_1 and crossover from σ_1 ~0 and $\sigma_2 < 0$ to $\sigma_1 > 0$ and $\sigma_2 > 0$ near T_{SMT} are indicative of the percolative nature of the carrier transport in VO_2 films near its phase transition [38], where both semiconducting and metallic phases coexist. It is clearly illustrated in Fig. 6A by the divergence of the real part of the dielectric function (ε_1), which is related to the imaginary part of the conductivity as expressed by Eq. (4).

$$\tilde{\sigma}(\omega) = \sigma_1(\omega) + i\sigma_2(\omega) = -i\varepsilon_0\omega(\tilde{\varepsilon}(\omega) - 1) \tag{4}$$

The changes in σ_1 (ε_2) and σ_2 (ε_1) agree with previous reports [14,33]. When the temperature varies from 59 °C to 63 °C, ε_2 increases from 70 to 750 while the ε_1 value increases from below 10 up to 180. At higher temperatures, ε_2 saturates at 750, while the sign of ε_1 changes at 65 °C, its value finally saturating at a value of −75 for $T > 72$ °C.

3.4. Conductivity models and the Drude-Smith formalism

Various attempts of analyzing and modelling the THz conductivity spectra of VO_2 thin films were reported using the effective medium theory (EMT) [28,39,40], which is suggested by the presence of separated metallic and semiconducting phases in the films. The lack of consistency of the results reported from such analysis arises from the difficulty of EMT to accurately model the behavior of the far-infrared conductivity in the vicinity of the SMT by simply using the optical constants of semiconducting and metallic phases [41]. Indeed, the properties of the newly-formed metallic puddles at the onset of the transition and those of the high temperature metallic phase are observed to differ. The properties of the metallic

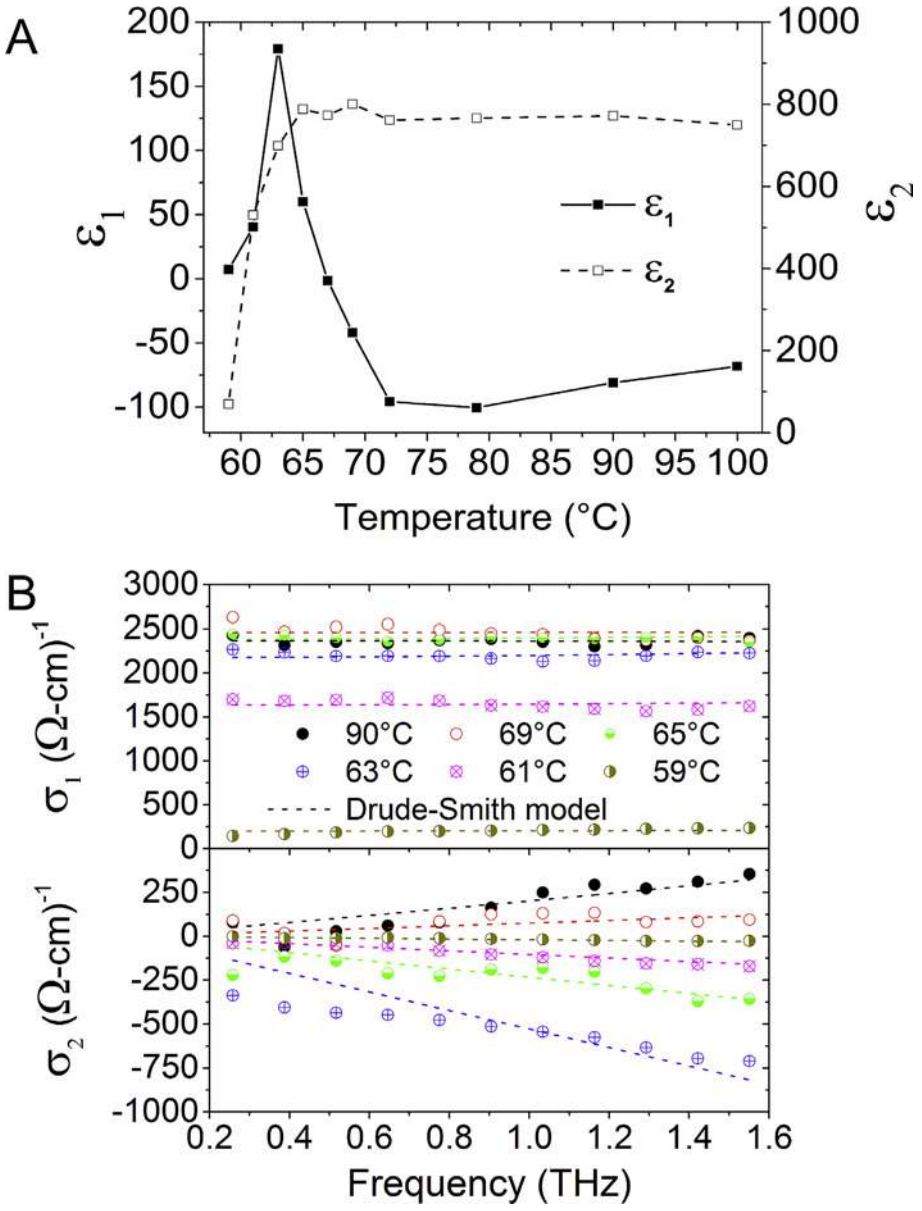

Fig. 6. (A) Temperature-dependent real (closed squares and solid line) and imaginary (open squares and dashed line) components of the permittivity of the VO_2 film at 1 THz across and above the phase transition during the heating segment. (B) Simultaneous fits of the real (upper panel) and imaginary (lower panel) parts of the terahertz conductivity of the VO_2 film through the phase transition using the Drude-Smith model (dotted lines).

puddles in the semiconducting host are reported to be analogous to those of a strongly correlated metal as opposed to the Drude-like feature of the high temperature metallic phase [14].

A better description of the complex THz conductivity of semiconductors, where disorder can result in carrier localization, was proposed using conductivity models derived from the Drude model [42]. These models mostly describe an inductive-type response and have two characteristic features: 1) σ_1 decreases with frequency and 2) σ_2 is positive and maximum near the frequency corresponding to the scattering rate [43]. However, the THz conductivity spectra of many semiconductor/dielectric or metallic/dielectric nanocomposites materials exhibit a capacitive response at low frequency, resulting in increasing σ_1 and in negative σ_2. In this case, the effect of local fields on a length scale much smaller than the wavelength of the probing radiation starts to play a significant role and the effective conductivity response differs from the microscopic conductivity of closely packed nanoparticles. For this particular type of nanomaterials, that includes materials near SMT and various nanostructured conducting systems, the Drude–Smith model [44] has been successfully used by many groups to explain the behavior of the frequency-dependence of the conductivity at THz frequencies [29,45–47]. This model is a classical generalization of the Drude model in the sense that a non-isotropic carrier diffusion term is introduced in the conductivity equation. A common assumption of the model is that the persistence of carrier's velocity is retained for only one collision. The Drude-Smith conductivity expression is then given by:

$$\tilde{\sigma}(\omega) = \frac{ne^2\tau_{DS}}{m^*}\left(\frac{1}{1-i\omega\tau_{DS}}\right)\left(1+\frac{c}{1-i\omega\tau_{DS}}\right) \tag{5}$$

where n is the carrier density, τ_{DS} is the Drude–Smith scattering time, m^* is the effective mass of the carriers and c is a parameter that can vary between 0 for Drude-type response and -1 for strong charge carrier localization at zero frequency. Within this model, carrier localization is associated with two parameters: 1) c that is an indicator of the degree of localization and 2) τ_{DS} that depends on the number of scattering events [29,48].

The non Drude-type conductivity response observed across the SMT and the nanogranular surface morphology of our epitaxially-

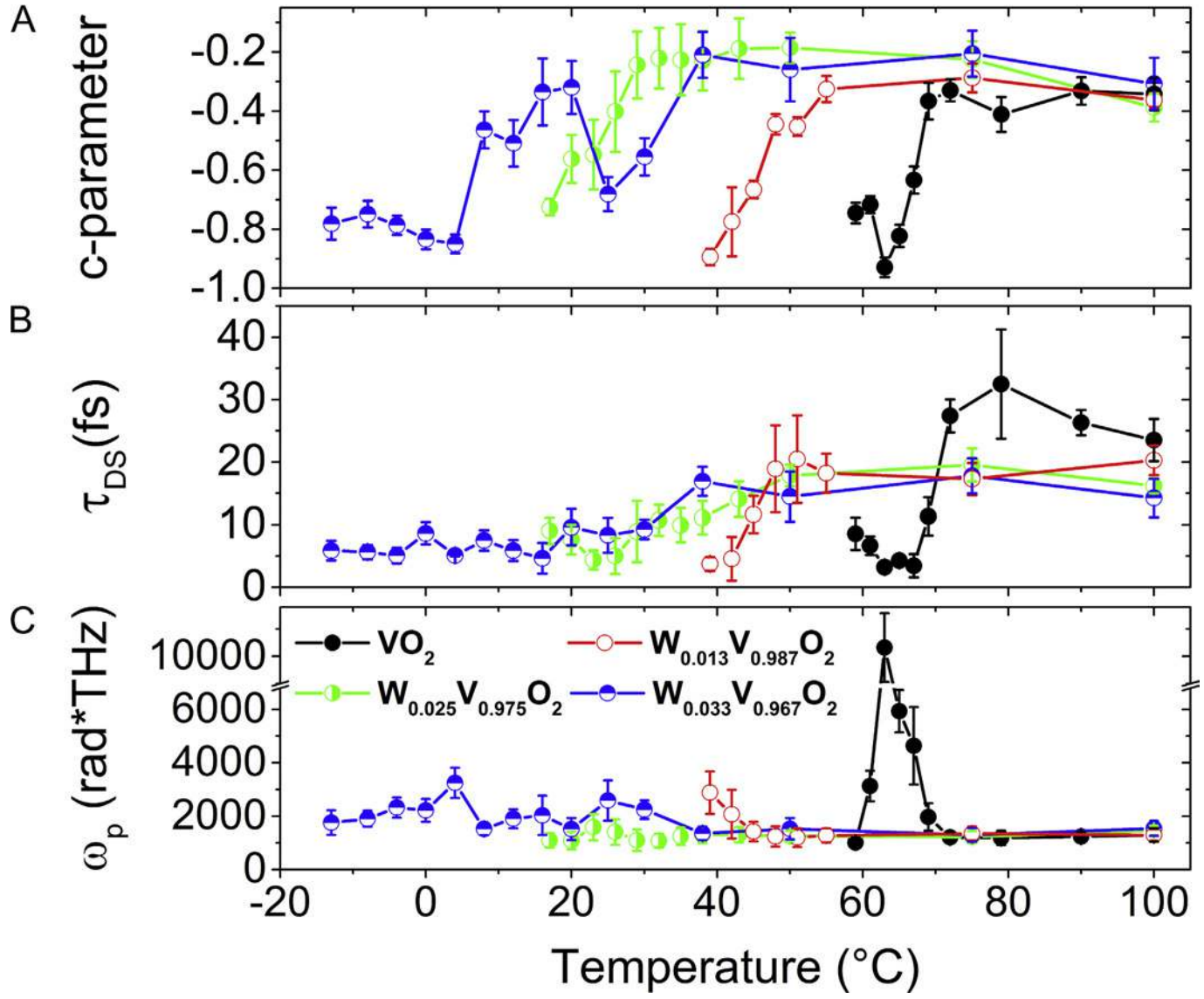

Fig. 7. Temperature dependence of the $W_xV_{1-x}O_2$ thin films Drude-Smith parameters (A) c parameter, (B) scattering time (τ_{DS}) and (C) plasma frequency (ω_p).

grown $W_xV_{1-x}O_2$ thin films suggest to use the Drude-Smith formalism to model the far-infrared temperature-dependent complex conductivity of $W_xV_{1-x}O_2$ samples. This model is well suited to the description of carrier transport in nanostructured systems in the presence of disorder related to carrier scattering mechanisms on grain boundaries. It has been used to describe the THz complex conductivity curves across the W-doped VO_2 phase transition with a limited number of fitting parameters. The fitting provides access to the carrier scattering time τ_{DS}, the plasma frequency ($\omega_p = \sqrt{ne^2/m^*\varepsilon_0}$) and the c parameter. The dotted lines in Fig. 6B correspond to the best fits of the conductivity data over the 0.25–1.55 THz spectral range. A slight deviation between the experimentally-determined and best-fitted values of σ_2 at T = 63 °C for low frequencies is observed not only because it corresponds to the temperature range where the changes in the THz conductivity is the largest but also because the Drude-Smith model requires that the value of $\sigma_2 = 0$ at f = 0 THz. The temperature dependence of the Drude-Smith fitting parameters (c, τ_{DS} and ω_p) obtained by fitting the conductivity data over 0.25–1.55 THz spectral ranges for the $W_xV_{1-x}O_2$ films is presented in Fig. 7. By increasing the temperature, so as to cross the phase transition region, it is observed for each film that c decreases from −0.35 to −0.80 while τ_{DS} decreases by a factor of 2. The plasma frequency is nearly temperature-independent, except at the onset of the transition, where a sharp jump of ω_p is observed. For $T > T_{SMT}$, $c \approx -0.35$ and $\omega_p \approx 1500$ rad THz for all the $W_xV_{1-x}O_2$ films. The scattering time is also constant above T_{SMT}, the highest values of τ_{DS} (≈25 fs) being obtained for the VO_2 film. The larger variation observed in the values of the c - parameter for the $W_{0.033}V_{0.967}O_2$ film as compared to the other $W_xV_{1-x}O_2$ films originates from its larger W content, which expands the range of temperatures over which both semiconducting and metallic phases coexist. The $W_{0.033}V_{0.967}O_2$ film thus remains in the region where the electronic response changes ($c \sim -0.5$) from inductive ($\sigma_2 > 0$) to capacitive ($\sigma_2 < 0$) on a wide range of temperature (5 °C < T < 40 °C). Within this transition region, small variations in the slope of σ_2 can significantly modify the calculated value of the c-parameter, for which $c > -0.5$ when the slope of σ_2 is positive and $c < -0.5$ when the slope of σ_2 is negative. Accordingly, the sensitivity of the fit to any small change in the slope of σ_2 increases. Because the phase transition occurs on a larger range of temperature for the $W_{0.033}V_{0.967}O_2$ film than for the other $W_xV_{1-x}O_2$ films, it exhibits a larger variation of the c - parameter value within the phase transition region. Both the values of plasma frequency and scattering time ($\omega_p = 1400$ rad THz and $\tau_{DS} = 23.5$ fs) obtained above T_{SMT} (T = 100 °C) are similar to those reported for VO_2 thin films deposited on Al_2O_3(1–102) substrate ($\omega_p = 2495$ rad THz and $\tau_{DS} = 8.0$ fs) [49]. The plasma frequency is related to the carrier density and the carrier effective mass, which both vary across the SMT. According to Hall-effect measurements, the carrier density in VO_2 increases by ~ 10^4 across the SMT [50] while according to optical measurements, the effective mass of the carriers is $m^* \sim 2m_e$ above the transition temperature [51]. For VO_2 at 100 °C and considering $m^* = 2m_e$, the carrier density calculated from the plasma frequency is $n \approx 1.04 \times 10^{21}$ cm^{-3} while calculation of the mobility of the carriers from $\tau_{DS} = \frac{m^*\mu}{(1+c)e}$ gives $\mu \approx 13.6$ cm^2/V s, which are both similar to values reported from THz-TDS spectroscopy measurements [29,41].

4. Discussion

Above the phase transition temperature, long-range carrier transport between well connected metallic VO_2 grains is expected. For temperatures slightly lower than T_{SMT} though, a more localized behavior is expected with strongly impeded macroscopic mobility: small-range carrier transport is allowed but grain boundaries limit long-range carrier transport due to the presence of semiconducting VO_2 barriers between the metallic nanograins [14,28,41]. As depicted in Fig. 6B, the semiconductor-to-metal transition is accompanied by an increase of σ_1 from a small to a large positive value and by a change in the slope of low frequency values of σ_2 from negative to positive. This characterizes the transition from a low temperature insulating regime to a high temperature conducting regime. In the temperature range corresponding to the width of the phase transition, the coexistence of both semiconducting and metallic phases leads to a change in the slope of σ_2 from positive to negative. According to the Drude-Smith model, this corresponds to a transition from an inductive electronic response ($c > -0.5$) to a capacitive electronic response ($c < -0.5$) [47]. Within this transitional regime, charge carriers are confined in the randomly dispersed emerging metallic $W_xV_{1-x}O_2$ nm-scale puddles and both the inhomogeneity of the material and the scattering at grain boundaries increase.

The relation between the transition of the electronic response from inductive to capacitive and the nature of the percolation threshold for $W_xV_{1-x}O_2$ films close to the SMT can be demonstrated by analogy with a simple 2-D pattern composed of metallic structures called metallic checkerboard pattern (MCP) [16,36]. For these patterns, significant changes in the electromagnetic response occurs depending on whether the adjacent metallic structures are connected (inductive MCP) or not (capacitive MCP). In both the metallic and semiconducting phases, an inductive regime is expected since the VO_2 film acts as a resistor in series with an inductor, for which the current lags behind the applied electric field ($\sigma_1 > 0$ and $\sigma_2 > 0$), the resistor contribution being smaller in the metallic phase. As temperature increases between these two inductive regimes (59 °C ≤ T ≤ 63 °C), individual VO_2 nanograins gradually undergo the SMT, resulting in an enhancement of the f_M/f_{S-C} ratio, where f_M and f_{S-C} are the metallic and semiconducting fractions of the VO_2 film respectively. The variation of both the value of τ_{DS} and the c parameter observed across the SMT is consistent with a reduced number of scattering events at metallic grain boundaries. At the onset of the SMT, the metallic puddles are limited in number and most of them do not connect with each other. They thus interact individually with the THz beam and contribute to a noticeable increase of ε_2 and ε_1, as observed in Fig. 6A. From the presence of these arbitrarily dispersed metallic puddles, a structure similar to the capacitive MCP emerges. Even though there is no periodicity in the position of the non-connected metallic structures in the film, a capacitive response is observed, in accordance with the natural disordered metamaterial behavior testified by the presence of a peak in $\varepsilon_1(T)$. As the temperature further increases ($T > 63$ °C), these metallic VO_2 grains grow in both size and number and coalesce until the percolation threshold is reached. At that point, the metallic structures connect together and the structure is assimilated to an inductive MCP. Therefore, the electronic response of the system switches back to inductive and the c parameter remains constant to a small value of −0.35 at higher temperature.

The emergence of the metallic puddles also gives rise to the peak observed in ω_p for the $W_xV_{1-x}O_2$ films at the onset of the SMT (see Fig. 7C). The electron density (n) of these puddles locally increases as they undergo the SMT and their initial growth in size is accompanied by a sharp change of the carrier effective mass (m^*). Similar behavior was theoretically predicted for an ensemble of metallic wires embedded in a dielectric media [52], for which m^* varies like $nr^2 \ln(a/r)$, with r the wire diameter and a the period of the array. A significant enhancement of ω_p, which varies like

$1/a^2 \ln(a/r)$, is thus expected right at the onset of this phase transition. As the metallic puddles coalesce, the carrier effective mass recovers a normal value and the plasma frequency reaches a constant value of ≈1500 rad THz.

The more pronounced increase in ω_p for the VO_2 film (up to ≈ 10000 rad THz) in comparison to the W-doped films (up to ≈ 1600−3300 rad THz) is mainly the consequence of the inhomogeneous insertion of W dopants in the VO_2 lattice. These W dopants not only increase the density of carriers in the semiconducting phase but also induce a wider stoichiometry distribution and structural distortions into the $W_xV_{1-x}O_2$ lattice, leading to a reduction of the grain size and of the corresponding wire radius. This results in a smaller enhancement in ω_p close to the SMT, a lower T_{SMT} and a widening of the temperature range over which the transition occurs [53], as it is also observed for τ_{DS} and c parameters. Moreover, smaller grain size results in larger density of defects and grain boundaries, thus reducing the electrons mean free path, the time between collisions and the scattering time in the metallic state of W-doped VO_2 (τ_{DS} ≈ 17 fs) as compared to that of VO_2 (τ_{DS} ≈ 25 fs).

5. Conclusions

In conclusion, the VO_2 first-order phase transition was probed in epitaxially-grown $W_xV_{1-x}O_2$ ($0 \leq x \leq 0.033$) films from complex conductivity measurements using THz-TDS and was successfully described using Drude-Smith formalism. It involves the gradual nucleation and percolation of metallic nanograins dispersed in a semiconducting host as temperature increases and it is accompanied by large variations of plasma frequency, scattering time and c parameter. These variations are induced by changes of the electronic response of the material from strongly capacitive to inductive and to a high degree of disorder in the vicinity of the phase transition. The non-zero value of the c parameter in both states is indicative of strong carrier confinement and of an inhomogeneous system where scattering occurs at defects and grain boundaries due to the nanogranular morphology of the films. Moreover, the emergence of the VO_2 metallic inclusions, with size much smaller than the probing wavelength, among a semiconducting host leads to the observed behavior of natural disordered metamaterial for the $W_xV_{1-x}O_2$ films close to T_{SMT}. In addition, doping VO_2 with W atoms enlarges the distribution of grain stoichiometry and structural distortion and reduces the grain size, leading to a larger density of defects and grain boundaries. Consequently, the carrier scattering time in the metallic state is reduced as compared with that of VO_2, the onset temperature of the SMT is lowered and the temperature range over which the metallic domains emerge and coalesce to form the high temperature metallic state is extended. The exploitation of $W_xV_{1-x}O_2$ films properties, which displays a change in their electromagnetic response close to room temperature, thus paves the way for a reduction in the complexity of the design of tunable metamaterials.

Acknowledgements

The authors are grateful to the Canada Research Chair program and the "Fonds de recherche du Québec − Nature et technologies (FRQNT)" for their financial support. We thank Prof. A. Hendaoui for insightful discussion regarding the interpretation of the results.

References

[1] D.R. Smith, J.B. Pendry, M.C.K. Wiltshire, Metamaterials and negative refractive index, Science 305 (2004) 788−792.
[2] S. Zhang, W. Fan, N.C. Panoiu, K.J. Malloy, R.M. Osgood, S.R.J. Brueck, Experimental demonstration of near-infrared negative-index metamaterials, Phys. Rev. Lett. 95 (2005), 137404.
[3] R.A. Shelby, D.R. Smith, S. Schultz, Experimental verification of a negative index of refraction, Science 292 (2001) 77−79.
[4] J.B. Pendry, D. Schurig, D.R. Smith, Controlling electromagnetic fields, Science 312 (2006) 1780−1782.
[5] Z. Liu, H. Lee, Y. Xiong, C. Sun, X. Zhang, Far-field optical hyperlens magnifying sub-diffraction-limited objects, Science 315 (2007) 1686.
[6] H.-T. Chen, W.J. Padilla, M.J. Cich, A.K. Azad, R.D. Averitt, A.J. Taylor, A metamaterial solid-state terahertz phase modulator, Nat. Phot. 3 (2009) 148−151.
[7] Y.H. Fu, A.Q. Liu, W.M. Zhu, X.M. Zhang, D.P. Tsai, J.B. Zhang, T. Mei, J.F. Tao, H.C. Guo, X.H. Zhang, J.H. Teng, N.I. Zheludev, G.Q. Lo, D.L. Kwong, A micromachined reconfigurable metamaterial via reconfiguration of asymmetric split-ring resonators, Adv. Funct. Mater 21 (2011) 3589−3594.
[8] K. Fuchi, A.R. Diaz, E.J. Rothwell, R.O. Ouedraogo, J. Tang, An origami tunable metamaterial, J. Appl. Phys. 111 (2012), 084905.
[9] T. Driscoll, H.-T. Kim, B.-G. Chae, B.-J. Kim, Y.-W. Lee, N.M. Jokerst, S. Palit, D.R. Smith, M. Di Ventra, D.N. Basov, Memory metamaterials, Science 325 (2009) 1518−1521.
[10] V. Eyert, The metal-insulator transitions of VO_2: a band theoretical approach, Ann. Phys. 11 (2002) 650−702.
[11] A. Zylberstejn, N.F. Mott, Metal-insulator transition in vanadium dioxide, Phys. Rev. B 11 (1975) 4383−4395.
[12] F.J. Morin, Oxides which shows a metal-to-insulator transition at the Neel temperature, Phys. Rev. Lett. 3 (1959) 34−36.
[13] H.W. Verleur, A.S. Barker, C.N. Berglund, Optical properties of VO_2 between 0.25 and 5 eV, Phys. Rev. 172 (1968) 788−798.
[14] M.M. Qazilbash, M. Brehm, B.-G. Chae, P.-C. Ho, G.O. Andreev, B.-J. Kim, S.J. Yun, A.V. Balatsky, M.B. Maple, F. Keilmann, H.-T. Kim, D.N. Basov, Mott transition in VO_2 revealed by infrared spectroscopy and nano-imaging, Science 318 (2007) 1750−1753.
[15] L. Wang, I. Novikova, J.M. Klopf, S. Madaras, G.P. Williams, E. Madaras, J. Lu, S.A. Wolf, R.A. Lukaszew, Distinct length scales in the VO_2 metal-insulator transition revealed by bi-chromatic optical probing, Adv. Opt. Mater 2 (2014) 30−33.
[16] K. Takano, F. Miyamaru, K. Akiyama, H. Miyazaki, M.W. Takeda, Y. Abe, Y. Tokuda, H. Ito, M. Hangyo, Crossover from capacitive to inductive electromagnetic responses in near self-complementary metallic checkerboard patterns, Opt. Express 22 (2014) 24787−24795.
[17] M.A. Kats, R. Blanchard, S. Zhang, P. Genevet, C. Ko, S. Ramanathan, F. Capasso, Perfect thermal emission and large broadband negative differential thermal emittance, Phys. Rev. X 3 (2013), 041004.
[18] C. Chen, Y. Zhao, X. Pan, V. Kuryatkov, A. Bernussi, M. Holtz, Z. Fan, Influence of defects on structural and electrical properties of VO_2 thin films, J. Appl. Phys. 110 (2011), 023707.
[19] D.H. Kim, H.S. Kwok, Pulsed laser deposition of VO_2 thin films, Appl. Phys. Lett. 65 (1994) 3188−3190.
[20] X. Tan, T. Yao, R. Long, Z. Sun, Y. Feng, H. Cheng, X. Yuan, W. Zhang, Q. Liu, C. Wu, Y. Xie, S. Wei, Unraveling metal-insulator transition mechanism of VO_2 triggered by tungsten doping, Sci. Rep. 2 (2012) 466.
[21] J.B. Goodenough, The two components of the crystallographic transition in VO_2, J. Solid State Chem. 3 (1971) 490−500.
[22] F.J. Wong, Y. Zhou, S. Ramanathan, Epitaxial variants of VO_2 thin films on complex oxide single crystal substrates with 3m surface symmetry, J. Cryst. Growth 364 (2013) 74−80.
[23] Y. Zhao, C. Chen, X. Pan, Y. Zhu, M. Holtz, A. Bernussi, Z. Fan, Tuning the properties of VO_2 thin films through growth temperature for infrared and terahertz modulation applications, J. Appl. Phys. 114 (2013), 113509.
[24] J. Jian, A. Chen, W. Zhang, H. Wang, Sharp semiconductor-to-metal transition of VO_2 thin films on glass substrates, J. Appl. Phys. 114 (2013), 224301.
[25] K. Shibuya, J. Tsutsumi, T. Hasegawa, A. Sawa, Fabrication and Raman scattering study of epitaxial VO_2 films on MgF_2 (001) substrates, Appl. Phys. Lett. 103 (2013), 021604.
[26] A. Chen, Z. Bi, W. Zhang, J. Jian, Q. Jia, H. Wang, Textured metastable VO_2 (B) thin films on $SrTiO_3$ substrates with significantly enhanced conductivity, Appl. Phys. Lett. 104 (2014), 071909.
[27] Y. Zhao, J.H. Lee, Y. Zhu, M. Nazari, C. Chen, H. Wang, A. Bernussi, M. Holtz, Z. Fan, Structural, electrical, and terahertz transmission properties of VO_2 thin films grown on c-, r-, and m-plane sapphire substrates, J. Appl. Phys. 111 (2012), 053533.
[28] P.U. Jepsen, B.M. Fischer, A. Thoman, H. Helm, J.Y. Suh, R. Lopez, R.F. Haglund Jr., Metal-insulator phase transition in a VO_2 thin film observed with terahertz spectroscopy, Phys. Rev. B 74 (2006), 205103.
[29] T.L. Cocker, L.V. Titova, S. Fourmaux, H.-C. Bandulet, D. Brassard, J.-C. Kieffer, M.A. El Khakani, F.A. Hegmann, Terahertz conductivity of the metal-insulator transition in a nanogranular VO_2 film, Appl. Phys. Lett. 97 (2010), 221905.
[30] H.W. Liu, L.M. Wong, S.J. Wang, S.H. Tang, X.H. Zhang, Effect of oxygen stoichiometry on the insulator-metal phase transition in vanadium oxide thin films studied using optical pump-terahertz probe spectroscopy, Appl. Phys. Lett. 103 (2013), 151908.
[31] A. Pashkin, C. Kübler, H. Ehrke, R. Lopez, A. Halabica, R.F. Haglund Jr., R. Huber, A. Leitenstorfer, Ultrafast insulator-metal phase transition in VO_2 studied by multiterahertz spectroscopy, Phys. Rev. B 83 (2011), 195120.
[32] M. Mao, W.-X. Huang, Y.-X. Zhang, J.-Z. Yan, Y. Luo, Q.-W. Shi, J.-H. Cai, Study

on phase transition property of tungsten-doped vanadium dioxide thin film at terahertz range, J. Inorg. Mater 27 (2012) 891–896.
[33] G. Karaoglan-Bebek, M.N.F. Hoque, M. Holtz, Z. Fan, A.A. Bernussi, Continuous tuning of W-doped VO_2 optical properties for terahertz analog applications, Appl. Phys. Lett. 105 (2014), 201902.
[34] N. Émond, A. Hendaoui, M. Chaker, Low resistivity $W_xV_{1-x}O_2$-based multilayer structure with high temperature coefficient of resistance for microbolometer applications, Appl. Phys. Lett. 107 (2015), 143507.
[35] M. Tinkham, Energy gap interpretation of experiments on infrared transmission through superconducting films, Phys. Rev. 104 (1956) 845–846.
[36] J. Lloyd-Hughes, T.-I. Jeon, A review of the terahertz conductivity of bulk and nano-materials, J. Infrared Milli. Terahz. Waves 33 (2012) 871–925.
[37] J.F. O'Hara, W. Withayachumnankul, I. Al-Naib, A review on thin-film sensing with terahertz waves, J. Infrared Milli. Terahz. Waves 33 (2012) 245–291.
[38] M. Walther, D.G. Cooke, C. Sherstan, M. Hajar, M.R. Freeman, F.A. Hegmann, Terahertz conductivity of thin gold films at the metal-insulator percolation transition, Phys. Rev. B 76 (2007), 125408.
[39] P. Mandal, A. Speck, C. Ko, S. Ramanathan, Terahertz spectroscopy studies on epitaxial vanadium dioxide thin films across the metal-insulator transition, Opt. Lett. 36 (2011) 1927–1929.
[40] D.J. Hilton, R.P. Prasankumar, S. Fourmaux, A. Cavalleri, D. Brassard, M.A. El Khakani, J.-C. Kieffer, A.J. Taylor, R.D. Averitt, Enhanced photosusceptibility near T_c for the light-induced insulator-to-metal phase transition in vanadium dioxide, Phys. Rev. Lett. 99 (2007), 226401.
[41] J. Lourembam, A. Srivastava, C. La-o-vorakiat, H. Rotella, T. Venkatesan, E.E.M. Chia, New insights into the diverse electronic phases of a novel vanadium dioxide polymorph: a terahertz spectroscopy study, Sci. Rep. 5 (2015) 9182.
[42] T.-I. Jeon, D. Grischkowsky, Nature of conduction in doped silicon, Phys. Rev. Lett. 78 (1997) 1106–1109.
[43] M.C. Beard, G.M. Turner, C.A. Schmuttenmaer, Transient photoconductivity in GaAs as measured by time-resolved terahertz spectroscopy, Phys. Rev. B 62 (2000) 15764–15777.
[44] N. Smith, Classical generalization of the Drude formula for the optical conductivity, Phys. Rev. B 64 (2001), 155106.
[45] H. Ahn, Y.-P. Ku, Y.-C. Wang, C.-H. Chuang, S. Gwo, C.-L. Pan, Terahertz spectroscopic study of vertically aligned InN nanorods, Appl. Phys. Lett. 91 (2007), 163105.
[46] D.G. Cooke, A.N. MacDonald, A. Hryciw, J. Wang, Q. Li, A. Meldrum, F.A. Hegmann, Transient terahertz conductivity in photoexcited silicon nanocrystal films, Phys. Rev. B 73 (2006), 193311.
[47] A. Thoman, A. Kern, H. Helm, M. Walther, Nanostructured gold films as broadband terahertz antireflection coatings, Phys. Rev. B 77 (2008), 195405.
[48] H. Nemec, P. Kužel, V. Sundström, Far-infrared response of free charge carriers localized in semiconductor nanoparticles, Phys. Rev. B 79 (2009), 115309.
[49] Y. Zhu, Y. Zhao, M. Holtz, Z. Fan, A.A. Bernussi, Effect of substrate orientation on terahertz optical transmission through VO_2 thin films and application to functional antireflection coatings, J. Opt. Soc. Am. B 29 (2012) 2373–2378.
[50] D. Ruzmetov, D. Heiman, B.B. Claflin, V. Narayanamurti, S. Ramanathan, Hall carrier density and magnetoresistance measurements in thin-film vanadium dioxide across the metal-insulator transition, Phys. Rev. B 79 (2009), 153107.
[51] H.S. Choi, J.S. Ahn, J.H. Jung, T.W. Noh, D.H. Kim, Mid-infrared properties of a VO_2 film near the metal-insulator transition, Phys. Rev. B 54 (1996) 4621–4628.
[52] J.B. Pendry, A.J. Holden, W.J. Stewart, I. Youngs, Extremely low frequency plasmons in metallic mesostructures, Phys. Rev. Lett. 76 (1996) 4773–4776.
[53] B.G. Chae, H.T. Kim, Effects of W doping on the metal–insulator transition in vanadium dioxide film, Phys. B 405 (2010) 663–667.